Mechanical Performance of Novel UHPFRC Grouted SHS Tube-Sleeve Connection: Experiments, Numerical Simulation and Analytical Approaches

Zhenyu Huang[1,2,3](✉) and Weixiong Deng[1,2]

[1] Guangdong Provincial Key Laboratory of Durability for Marine Civil Engineering, Shenzhen University, Shenzhen 518060, China
`huangzhenyu@szu.edu.cn`

[2] Key Laboratory of Impact and Safety Engineering, Ministry of Education, Ningbo University, Ningbo 315211, China

[3] Key Laboratory for Resilient Infrastructures of Coastal Cities, Shenzhen University, Ministry of Education, Shenzhen 518060, China

Abstract. This paper presents the axial and lateral performance of a novel ultrahigh-performance fiber-reinforced concrete (UHPFRC) grouted SHS tube-Sleeve connection for prefabricated prefinished volumetric constructions (PPVC). The experimental study tested 18 full-scale specimens with varying shear key spacings, inner tube lengths, inner tube heights, and volume proportions of steel fiber in UHPFRC. The results showed that the connection have adequate resistance and ductility to resist tension and bending moment. The failure modes in tension mainly include the shear failure of the UHPFRC and the fracture of the inner tube, while the failure modes in bending mainly include the fracture of the inner tube and the slip of the grout. To further understand the load transfer mechanism of the connection, the advanced finite-element (FE) models were built to simulate the axial and lateral load–displacement behavior, strain and crack development of the grout. Thereafter, new design formulas are developed and evaluated to predict the axial and lateral resistance of the grouted connections. Validation against the test results showed that the new formulas can provide reasonably effective and accurate predictions of the axial-load and lateral-load resistance of the novel grouted connection.

Keywords: Grouted sleeve connection · UHPFRC · Axial-load resistance · Lateral-load resistance · Finite element analysis (FEA)

1 Introduction

Modular construction, by which the modules are prefabricated off-site and assembled on-site, has become a popular trend in construction industry due to its higher efficiency and productivity, better quality and safety, as well as lesser labor force and pollution. Depending on the degree of off-site manufacturing, the modular unit varies from simple

stick frame systems, like pre-cast concrete or prefabricated bathroom pods, up to fully prefabricated prefinished volumetric constructed (PPVC) module (Liew et al. 2019). As a special modular construction, PPVC pre-finishes the internal elements such as mechanical, plumbing and electrical, etc., before the installation of the modules and thus owns the highest prefabrication rate. One of the most critical issues affecting the integrity and safety of the modular building is the connection between the PPVC module (Dai Pang et al. 2016).

PPVC modules are normally connected externally for minimization of interior decoration on-site (Liew et al. 2019). According to the joint location, the connections are classified as corner connection, perimeter connection and interior connection. Although bolted connections are widely used, some critical issues still exist. Firstly, the accumulation of geometric and positioning deviations may easily cause alignment issues especially for the high-rise modular buildings (Generalova et al. 2016). Secondly, corrosion is a critical problem for bolted connections exposed to humid weather environment (Singapore and Authority 2017). Thirdly, the extensive usage of bolted connection would reduce the productivity of modular construction and cause collision problems during the assembly process (Sanches et al. 2018). To overcome these issues, a shear key-grouted column connection of square hollow section (SHS) has been proposed, which connects the upper column and lower column through the grout in the annulus of the connection (Huang et al. 2021; Sui et al. 2020). These investigations conclude that for the connection under axial compression, the load is transferred from the upper outer tube to the lower outer tube. The load resistance is dominated by the geometric sizes and material properties of the outer tubes. For the connection under axial tension, the load is transferred from the upper outer tube to the inner tube through the infilled grout. The failure mechanism is more complex and the load resistance is difficult to predict. Dai et al. (2021, 2020) conducted experimental and numerical studies on the axial and bending resistance of SHS column connections for modular construction, which effectively supplemented the availability of the connection. However, there is no analytical model of axial resistance and the number of lateral-load specimens is insufficient.

As a continuation and deeper investigation, the current study designs a novel SHS column connection, as shown in Fig. 1, which is an improvement of the column connection reported by Sui et al. (2020). Then the study tests ten full-scale specimens under axial tension and eight specimens under lateral compression to examine the failure modes and load resistances. Then, advanced FE simulation is performed to get more information on the stress and crack development of the infilled grout. Finally, two analytical models are proposed to predict the axial and lateral resistance of SHS column connections. Among them, the axial analytical model considers the influence of section shape and bond slip, while the lateral analytical model is calculated based on the elastic-plastic design theory.

2 Experimental Programme

2.1 Material Properties

To check the influence of material properties on the failure mode and load resistance of the column connection, three types of UHPC with 0, 1 and 2% of steel fiber have been developed. To achieve the same level of compressive strength around 100 MPa, the three
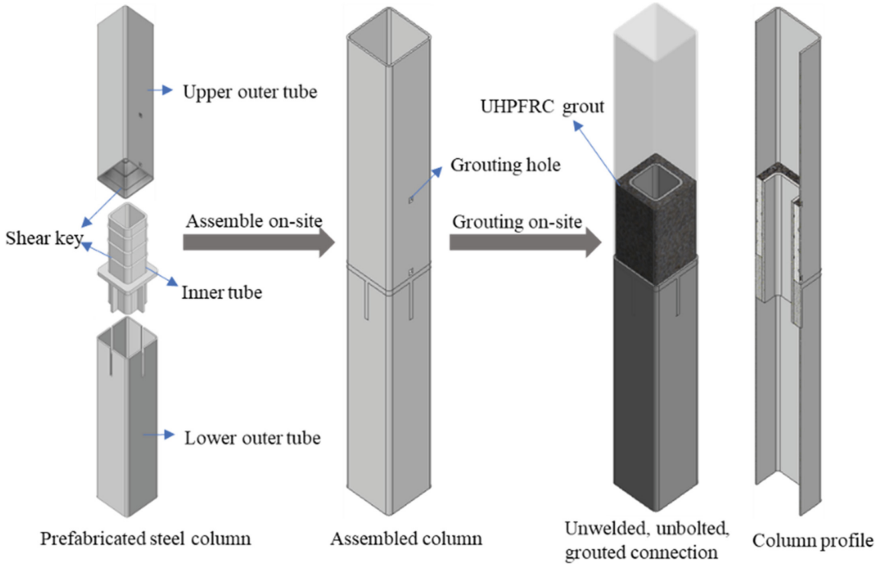
Fig. 1. Fabrication procedure of the column connection.

types of UHPC are designed with slightly different mix proportions, as shown in Table 1. The tensile strength and elastic modulus of fibers are around 2750 MPa and 200 GPa, respectively. For each mixture, the experimental program tests three $\Phi 100 \times 200$ mm concrete cylinders according to ASTM C39/C39M (International 1999) to determine the compressive strength, and five concrete coupons according to JSCE-2008 (Yokota et al. 2008) to determine the tensile strength. Table 2 lists the material properties of concrete. The compressive strength of the three types of UHPC are around 100 MPa.

The experimental program has extracted curved coupons from the corner region of the tubes, and flat coupons from the flat region of the tubes, as well as flat coupons from the steel plates. Table 3 summarizes the Young's modulus, 0.2% offset yield strength, and ultimate strength of the steel tubes, steel plates and rebars, respectively.

Table 1. Mix proportion of UHPFRC (kg/m³)

Mix	W/B	W	OPC	SF	GGBFS	S	F	HWRA	SRA
UHPC	0.19	209.5	823.3	135.5	170.1	1060.0	0	7.29	6.29
UHPFRC (1%)	0.21	213.9	750.0	130.5	165.1	1120.0	78.0	7.15	6.42
UHPFRC (2%)	0.24	229.1	705.0	120.5	155.1	1150.0	156.0	5.81	6.87

Notes W/B = water to binder ratio; W = water; OPC = ordinary Portland cement; SF = silica fume; GGBFS = mineral power; S = sand; F = steel fiber; HWRA = high Water reducing agent; SRA = shrinkage reducing agent; R = retarder

Table 2. Material properties of the concrete

Concrete	f_{cu} (MPa)	E_c (GPa)	f_t (MPa)	Poisson's ratio
UHPC	96.6	41.4	5.4	0.185
UHPFRC (1%)	105.8	42.6	6.0	0.182
UHPFRC (2%)	108.9	44.2	6.1	0.192

Table 3. Material properties of the steel components

Component	Material	E_s (GPa)	f_y (MPa)	f_u (MPa)
Inner tube flat	Mild steel	205.3	260.5	405.6
Inner tube corner		202.2	482.5	522.1
Outer tube flat		202.1	323.5	457.7
Outer tube corner		208.4	461.7	541.6
Steel plate		206.2	377.6	546.8
Shear key	HRB 400Φ6	193.6	357.0	485.0

2.2 Test Specimens

Figure 2 shows the configuration of the SHS column connection. Table 4 lists the geometric parameters of the 18 SHS column connections. The main geometric parameters include the outer diameter, thickness and radius of the round corner of the outer tube (B_o, t_o and r_o), the inner diameter, thickness and radius of the round corner of the inner
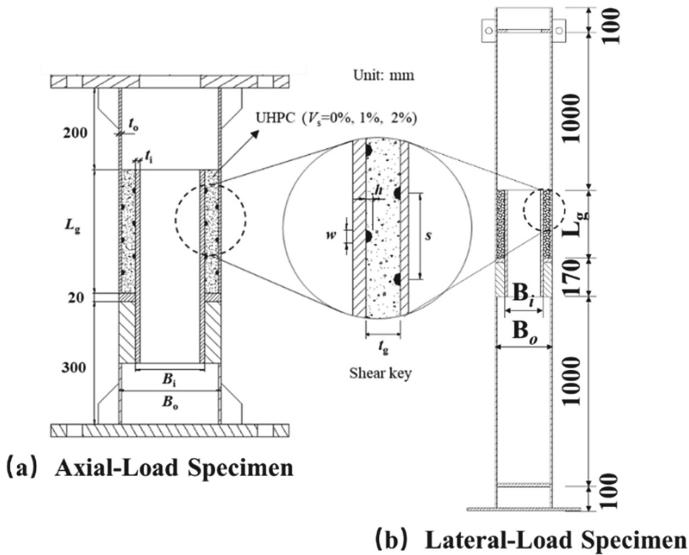

(a) Axial-Load Specimen

(b) Lateral-Load Specimen

Fig. 2. Configuration of the tube grouted connection.

tube (B_i, t_i and r_i), the length and thickness of the infilled grout (L_g and t_g), and the shear key spacing (s). The shear keys, in the form of steel bar with $w = 6$ mm height and $h = 12$ mm width, are welded to the both inner surface of the upper outer tube and the outer surface of the inner tube. These specimens vary with different shear key spacings ($s = 60$ mm, 80 mm, 120 mm), inner length ($B_i = 160$ mm, 170 mm, 180 mm), inner tube height ($L_g = 300$ mm, 360mm, 420 mm), and volume proportions of steel fiber ($V_s = 0\%$, 1%, 2%).

2.3   Test Set-Up, Loading and Measurement

Figure 3 shows the test set-up and Linear Variable Displacement Transducers (LVDTs) measurement scheme. Digital Image Correlation (DIC) technology is used for cross verification of lateral-load specimens. The experimental program adopts a computer-controlled servo hydraulic actuator with a load capacity of 5000 kN. The actuator applies an axial tensile force on the top of the specimen and a lateral force in the middle of the specimen through displacement control mode with a loading rate of 0.2 mm/min. The loading rate increases to 1 mm/min when the specimen starts to fail or the loading force starts to drop down.

3   Test Results

3.1   Failure Modes

Figure 4 (a) and (b) show the typical failure modes observed for SHS column connections under axial tension, while Figs. 4 (c) and (d) show failure modes under lateral load.

For the axial tension test, generally, if the grouted region is strong enough, the outer and inner tubes would yield and the inner tube may fracture at the intersection with the steel plate; if the grouted region is not stiff enough, the infilled grout would crush with obvious bond-slip between the upper outer tube and inner tube, and the steel tubes yield. The crack patterns are also classified into two types. The first type is the diagonal line crack linking the staggered two shear keys on the inner surface of the outer tube and the outer surface of the inner tube, respectively (Fig. 8). The two adjacent parallel diagonal line cracks form the compression strut, through which the load is transferred from the outer tube to the inner tube. The second type is the large-area crush along the outer surface of the inner tube. For the lateral load test, the concrete slip and inner tube fracture are the main failures. Firstly, the cracks of concrete are typically distributed in the tensile area of the connection, and the specimens S80T170L300V0-L have obvious shear cracks. In addition, the failure of most specimens is that the gap between the upper and lower column is open, and the inner tube reaches the fracture state. This may be due to the synergistic contradiction between the shear performance of UHPFRC and the fracture performance of steel.

3.2   Load-Displacement and Moment-Curvature Curves

Figure 5 displays the load-displacement curves of all the eighteen SHS column connections. P indicates the external load applied by the actuator, and δ indicates the vertical

Table 4. Geometric dimensions of test specimens

Specimen		$Bo \times to \times ro$ (mm × mm × mm)	$Bi \times ti \times ri$ (mm × mm × mm)	s (mm)	L_g (mm)	V_s (%)
Axial-loading	S80 T170L300F0-A	250 × 8 × 30	170 × 12 × 25	80	300	0
	S60 T170L300F0-A	250 × 8 × 30	170 × 12 × 25	60	300	0
	S120 T170L300F0-A	250 × 8 × 30	170 × 12 × 25	120	300	0
	S80T170L300F1-A	250 × 8 × 30	170 × 12 × 25	80	300	1
	S80T170L300F2-A	250 × 8 × 30	170 × 12 × 25	80	300	2
	S80T160L300F2-A	250 × 8 × 30	160 × 12 × 25	80	300	2
	S80T180L300F2-A	250 × 8 × 30	180 × 12 × 25	80	300	2
	S80T170L360F1-A	250 × 8 × 30	170 × 12 × 25	80	360	1
	S80T170L420F1-A	250 × 8 × 30	170 × 12 × 25	80	420	1
	S80T170L420F0-A	250 × 8 × 30	170 × 12 × 25	80	420	0
Lateral-loading	S120T170L300V1-L	250 × 8 × 30	170 × 12 × 25	120	300	1
	S80T170L300V1-L	250 × 8 × 30	170 × 12 × 25	80	300	1
	S80T170L300V0-L	250 × 8 × 30	170 × 12 × 25	80	300	0
	S60T170L300V1-L	250 × 8 × 30	170 × 12 × 25	60	300	1
	S80T160L300V1-L	250 × 8 × 30	160 × 12 × 25	80	300	1
	S80T180L300V1-L	250 × 8 × 30	180 × 12 × 25	80	300	1
	S80T170L360V1-L	250 × 8 × 30	170 × 12 × 25	80	360	1
	S80T170L420V1-L	250 × 8 × 30	170 × 12 × 25	80	420	1

(a) Axial-Load Specimen   **(b) Lateral-Load Specimen**
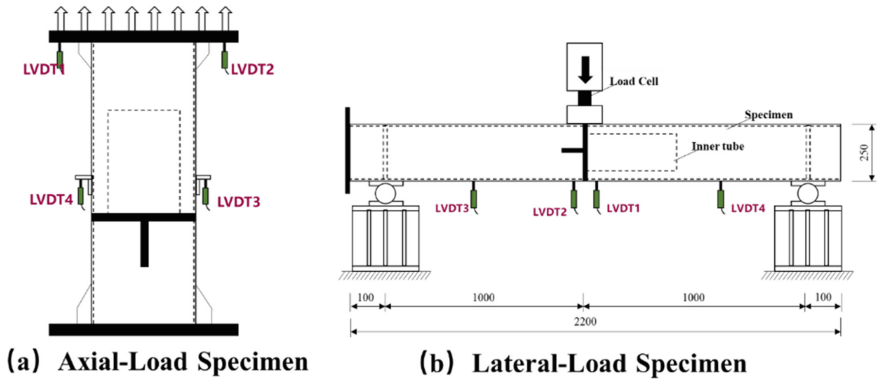
Fig. 3. Test setup and measurement scheme.

(a) Inner tube fracture and outer tube yielding

(b) Concrete crush

(c) Shear slip of concrete

(d) Inner tube fracture
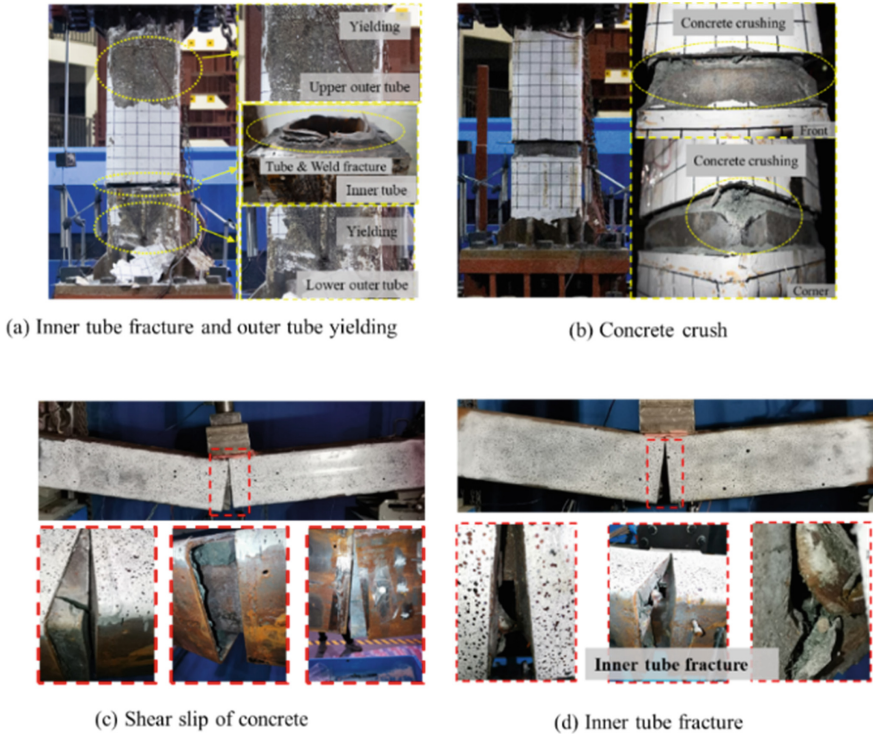
Fig. 4. Failure modes

displacement measured at the top end plate. For axial loading, the curve of external load to vertical displacement is drawn in Fig. 5 (a) - (b). For three-point bending, the curve of bending moment versus upper column curvature is shown in Fig. 5 (c) - (d). All the curves exhibit a similar trend before reaching the peak load resistance. The load-displacement relationship is initially elastic, and then enters into the nonlinear stage due to the crack

of the infilled grout. After reaching the peak load resistance, the curve drops down either due to the fracture of the inner tube or due to the crush of the infilled grout.

Under axial loading, the peak load resistance of the specimen is positively related to the strength of the grout. The specimen with the longest inner tube height, S80T170L420F0-A has the largest capacity at the grouted connection and the peak load resistance reaches 3005.2 kN. The specimen S80T170L420F1-A is supposed to have the same load level with S80T170L420F0-A. The specimen with the shortest inner tube height and largest shear key spacing, S120T170L300F0-A, has the smallest capacity at the grouted connection and the peak load resistance is only 1404.6 kN.

During lateral loading, there is a sharp decrease for bending moment except S80T170L300V0-L and S80T160L300V1-L. This is due to the fracture of the steel in the tensile area of the inner tube. Since the upper and lower limits of lateral bearing capacity are controlled by the section properties, S80T180L300V1-L and S80T160L300V1-L have the maximum and minimum resistance, which are 280.5 kN·m and 252.5 kN·m, respectively. Obviously, S80T170L300V0-L has superior ductility behavior compared with other specimens, thus 1% fiber addition may not be necessary. Moreover, the increase of the inner tube height results in a more significant fracture trend. The reason is that not only there are more shear keys within the grout to form more grout struts, but also the bond area between concrete and steel tube increases, which cumulatively increase plastic deformation. It is worth noting that for the whole connection, when fracture failure occurs, the connection is regarded as the limit state.
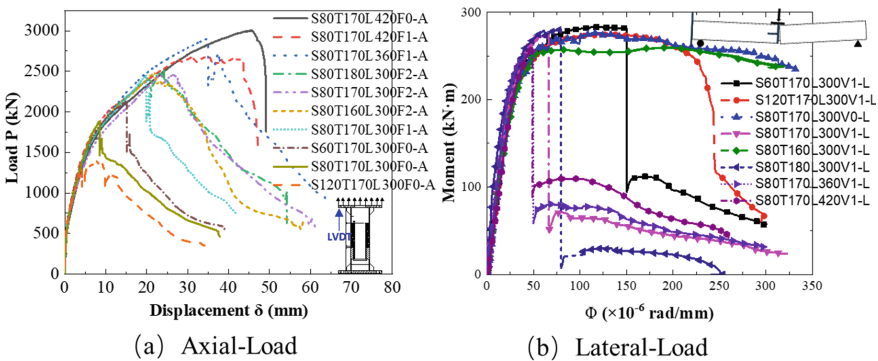

Fig. 5. Load-displacement and moment-curvature curves.

4   Finite Element Modelling

4.1   Material Model

The FE analysis adopts the concrete damage plasticity (CDP) model to represent the behavior of the UHPC and UHPFRC. The CDP model specifies the inelastic behavior of concrete as isotropic damaged elasticity in combination with isotropic tensile and

compressive plasticity. Sui et al. (2020) have discussed the compressive and tensile constitutive relationship for UHPFRC and UHPC, respectively, and plotted the nondimensional stresses-inelastic strain curves and nondimensional damage variables-inelastic strain curves, which are used in this study.

In ABAQUS, engineering stress and strain are transferred by inputting the trues stress and strain of steel. The fracture simulation in the three-point bending experiment requires specification of the relationship between the equivalent strain-to-fracture and stress triaxiality. ABAQUS provides several models to define the ductile damage, and this study adopts the Johnson–Cook criterion model. The fracture locus and failure parameters need to be calibrated by experiments (Zhang et al. 2020).

4.2   Validation of FE Model

Figures 6 and 7 compare the load–displacement curves of the 18 grouted connections obtained from the tests and FE simulations. The predictive load resistances are very close to the test values. When approaching the peak axial-load, a significant number of cracks are generated in the grout. The load resistance of the specimen is reduced due to the shear crushing of the grout, and the load–displacement curves show dramatic decreases. The strength of the grouted connection is negatively related to the shear key spacing and positively related to the inner tube height, as shown in Fig. 6(a) and (b). This is because the number of shear keys will affect the formation of compression struts bearing axial force in grouting. The load-displacement behavior and the peak load resistance of the three specimens are very close to each other, indicating that the inner tube length has marginal effect on the axial-load capacity of the SHS column connection, as shown in Fig. 6(c). The reason is that the increase of inner tube length only changes the angle of the compression strut, but does not change the number of shear keys and the contact area between the concrete and steel tubes.

Regarding the effect of steel fiber in concrete, the results obtained from axial-load specimens and lateral-load specimens are quite different. As shown in Figs. 6(d) and 7(d), grout containing fibers can improve ductility under axial loading, but lead to tube fracture under lateral loading. The development of inner tube fracture is mainly due to the opening of the outer tube of SHS column connection after lateral loading test, resulting in the fracture strain of the inner tube contributing to the lower limit of lateral resistance. As shown in Fig. 7(c), the moment-curvature curves show that the peak resistance increases only significantly with the increase of the inner tube area in the midspan section.

4.3   Development of Crack and Fracture

Compared with the test results, the validated FE model provides a convenient and useful tool to extract detailed information on the development of crack in the grout. For the axial-load specimens failed by grout shear crushing, the crack pattern in the grout initially was diagonal between two staggered shear keys on the inner surface of the outer tube and the outer surface of the inner tube. At the peak load, the diagonal line cracks developed rapidly, leading to severe crushing along the longitudinal direction and large bond-slip between grout and steel tubes. For the specimens in Fig. 8(i) and (j) with longer inner tube height, only minor diagonal line cracks formed and the grout was not crushed.
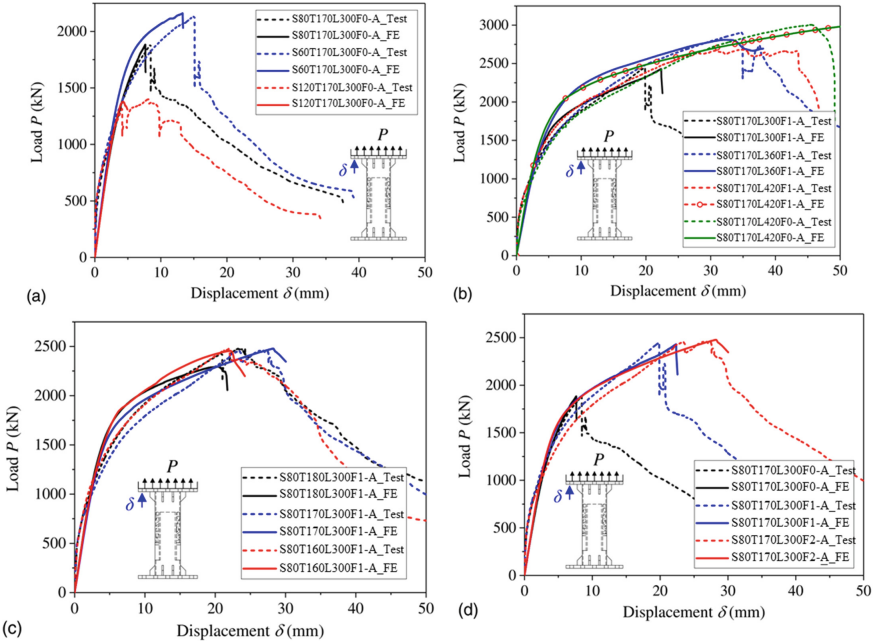
Fig. 6. Comparison of load–displacement curves under axial loading: (a) with different shear key spacing; (b) with different inner tube heights; (c) with different inner tube lengths; and (d) with different volume proportions of steel fiber.

Among the specimens with tube fracture, the concrete only develops diagonal damage in the area with the largest curvature, while the specimens with obvious bond slip are observed with damage at the diagonal of each shear key in the tensile area (Fig. 9). Generally, the proposed FE model was able to reproduce satisfactorily the damage in the grout observed from the tests.

5   Theoretical Model

5.1   Prediction of Axial-Load Resistance

5.1.1   Axial Load Resistance

To provide guidance for the design of UHPFRC grouted SHS tube sleeve connections, this section derives a theoretical model based on the load transfer mechanism of the sleeve connection to predict the axial-load resistance. The axial load resistance consists of the resistance contribution of the shear key interlock, friction and adhesion as given by:

$$P_u = 4B_i L_g \tau_u \tag{1}$$

where the ultimate shear stress can be obtained:
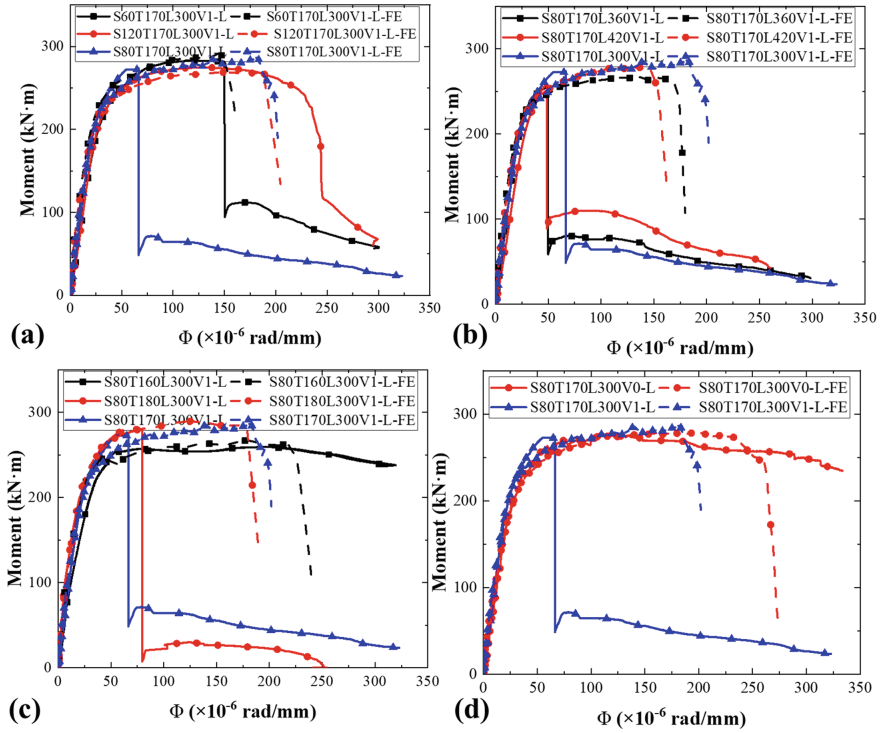
$$\tau_u = \tau_b + \tau_s \tag{2}$$

Fig. 7. Comparison of load–displacement curves under lateral loading: the meaning of (a) – (d) are the same as Fig. 6 (a) – (d).
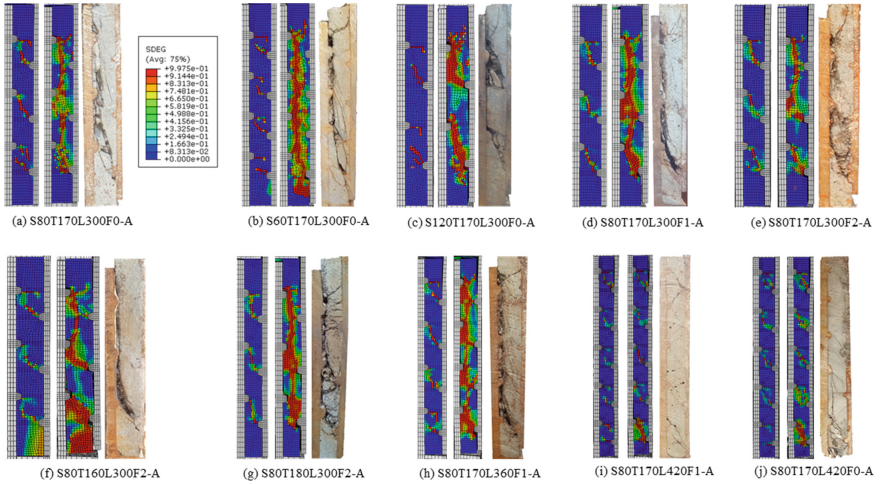

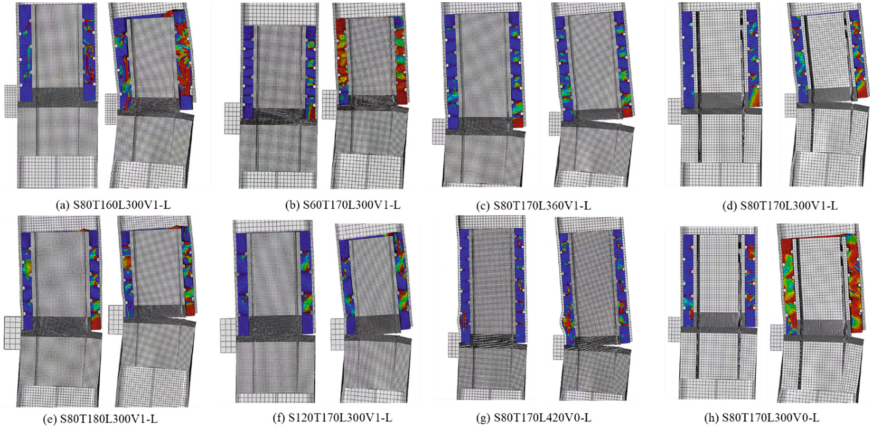**Fig. 8.** Development of crack in the grout under axial loading.

Fig. 9. Development of crack in the grout under lateral loading.

where τ_b is the bond strength due to friction and adhesion; τ_u is the ultimate shear strength; τ_s is the shear key interlock strength; B_i, h, s and L_g are the width of the inner tube, shear key height, shear key spacing, and height of inner tube, respectively.

(a) free body diagram of cracked compression strut   (b) critical triangular region

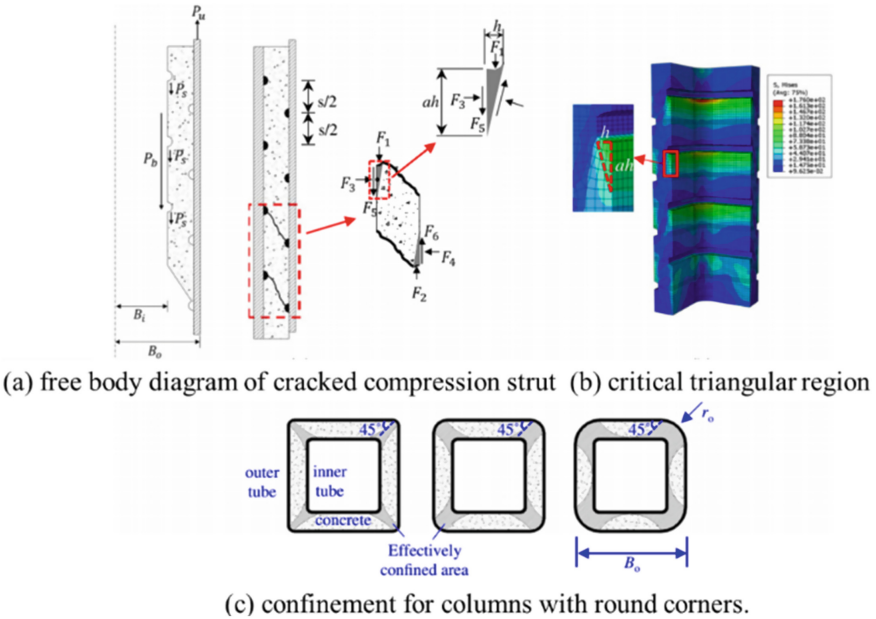(c) confinement for columns with round corners.

Fig. 10. Shear key interlock.

5.1.2 Friction and Adhesion for UHPFRC Grouted SHS Tube Sleeve Connection

Based on the previous study of the CHS concrete-filled steel tubes and SHS concrete-filled steel tubes reported by Lyu and Han (2019), an equation considering the shape effect is proposed:

$$\tau_{\mathrm{b}} = \left(0.043 + 0.028\frac{2r_{\mathrm{o}}}{B_{\mathrm{o}}}\right) + \left(1100 + 3800\frac{2r_{\mathrm{o}}}{B_{\mathrm{o}}}\right)\left(\frac{t_{\mathrm{o}}}{B_{\mathrm{o}}^2}\right) \tag{3}$$

where r_o is radius of the round corner of the outer tube; t_{o} is thickness of the outer tube.

5.1.3 Shear Key Interlock for SHS Column Connection

The shear strength contributed by the shear keys needs to be calculated according to the tension and compression strut model, as shown in Fig. 10(a). The effect of confined concrete needs to be considered. Therefore, the confined concrete model is adopted for the SHS connection confined by steel tubes with round corners, as shown in Fig. 10(c) (Wang and Wu 2008). Since the sharp square column has weak confining effect, the confined concrete strength for the sharp square column is assumed as $f_{\mathrm{cu}}^* = f_{\mathrm{cu}}$. Then, the shear strength contributed by the shear keys is given by:

$$\tau_{\mathrm{s}} = \frac{P_{\mathrm{s}}}{4B_{\mathrm{i}}L_{\mathrm{g}}} = \xi f_{\mathrm{cu}}\left(1 + \frac{h}{B_{\mathrm{i}}}\right)\frac{h}{s} = \left(1 + \frac{h}{B_{\mathrm{i}}}\right)\frac{h}{s}\frac{a}{a - \frac{8.2r_{\mathrm{o}}}{B_{\mathrm{o}}}R}f_{\mathrm{cu}} \tag{4}$$

where a is side length correction coefficient of critical triangle in grout (Fig. 10a); $n = L_{\mathrm{g}}/s$ is the number of shear keys; f_{cu}^* is the confined concrete strength; ξ is ratio of f_{cu}^* to f_{cu}; r_{o} is radius of the round corner of the outer tube.

5.2 Prediction of Lateral-Load Resistance

TO predict the bending moment of the grout connection, a fiber element model for composite structure is developed. To conservatively predict the load resistance, the section stress state is defined based on the elastic-plastic limit state.

5.2.1 Assumptions

To simplify the calculation and ensure the accuracy of the predictions, the following assumptions are adopted: (a) plane sections remain plane; (b) ignore the section corner radius; (c) strain-compatibility condition and (d) ignore the contribution of the area below both sides of the outer tube and the tensile area of the concrete (the part exceeding h_0). Three typical ultimate limit state design (ULSD) methods are taken into consideration as the failure criterion: (a) elastic; (b) elastoplastic; and (c) plastic method, which are shown in Fig. 12.

5.2.2 Constitutive Model

The stress-strain curves of UHPFRC and steel are shown in Fig. 11. This paper adopts the concrete model proposed by Wee et al. (1996) that can well represent the strain

softening behavior and post-peak behavior of concrete after the peak point. As a strain hardening material, based on simple mixing parameters, the rising stage and next stage of the UHPFRC uniaxial tensile stress-strain relationship can be analyzed by the study of Isa et al. (2021). As for structural steel, the perfect elastic-plastic model is used.
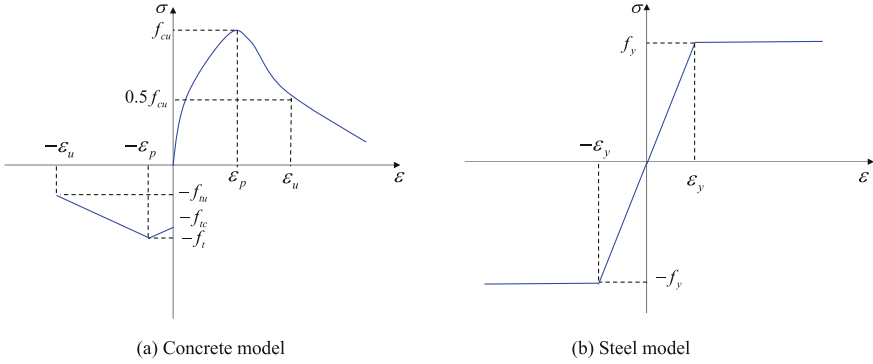

(a) Concrete model   (b) Steel model

Fig. 11. Constitutive models for martials.

5.2.3 Fiber Element Analysis

The composite section is divided into strip fiber elements. The stress distribution in each fiber element is calculated based on the plane section assumption and the material constitutive model. The current study focuses on the elastic-plastic limit state of the structure. Thus, the stress is distributed nonlinearly with the neutral axis of the section. It needs to be assumed that the material enters the plastic stage after the elastic stage. Generally speaking, when the concrete strain develops to the ultimate strain, the failure occurs (Fig. 12).
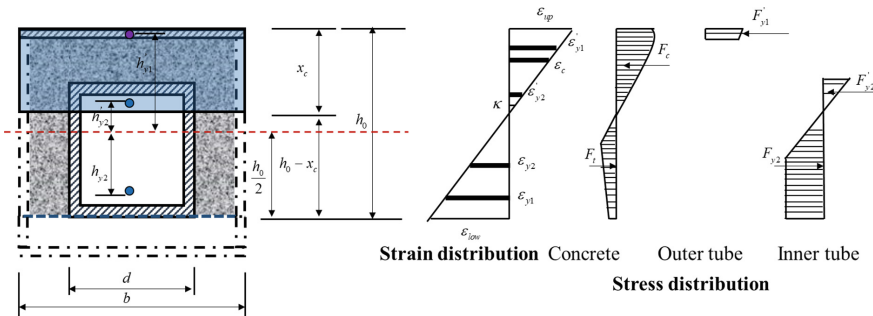

Strain distribution Concrete   Outer tube   Inner tube

Stress distribution

Fig. 12. Plane section assumption and force equilibrium of grout connection.

5.3 Validation

The validation of the proposed analytical model on the axial load resistance of SHS column connections adopts the test results of the ten specimens tested in this study and the four specimens tested by Dai et al. (2020).The verification of lateral load resistance adopts the test results of eight specimens in this study and two specimens tested by Dai et al. (2021). Figure 13 plots the ratios of the predicted results to the test results. The mean value of the ratios (axial-load and lateral-load) are 0.85 and 0.92 while these standard deviations are 0.12 and 0.13, respectively. Thus, the proposed analytical model is satisfactory to predict the axial and lateral load resistance of SHS column connections, and the prediction is relatively conservative for practical design.
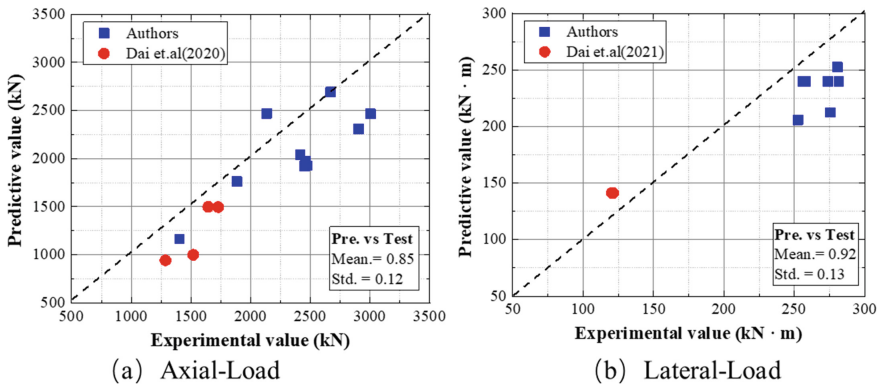

(a) Axial-Load   (b) Lateral-Load

Fig. 13. Test results and predicted results.

6 Conclusions

A novel UHPFRC grouted SHS tube sleeve connection was developed and its load resistance behaviour were investigated experimentally, numerically, and theoretically. The research work reported in the paper supports the following conclusions:

(1) Under axial loading, for the SHS column connection with sufficient strength of the grouted region, the connection fails by fracture of the inner tube at the intersection with the steel plate; for the SHS column connection with insufficient strength of the grouted region, the connection fails by bond-slip and concrete crush. Under lateral loading, the connection fails either by the fracture of the inner tube or bond slip between tube and concrete.

(2) The increase of steel fibre content and inner tube height can effectively improve the axial resistance of SHS column connection, but it will reduce the lateral ductility. The increase of inner tube length has little effect on the axial bearing capacity of SHS column connection, but it significantly improves the lateral bearing capacity.

(3) The FE model has successfully illustrated the load transfer mechanism of the SHS column connection under axial and lateral loading. It effectively reproduces the crack development, bond slip and fracture of inner tube in grouting.

(4) The proposed axial-load analytical model considered the effects of cross-section shape and corner radius on the strength of confined concrete. For the prediction of bending moment resistance of grout connection under lateral load, an elastic-plastic model based on the plan section assumption is proposed. The predictive load resistances agree well with the test values.

References

Dai Pang, S., Liew, J.Y.R.L., Dai, Z., Wang, Y.: Prefabricated prefinished volumetric construction joining techniques review. In: Modular and Offsite Construction (MOC) Summit Proceedings, pp. 2562–5438 (2016)

Dai, Z., Cheong, T.Y.C., Dai Pang, S., Liew, J.Y.R.: Experimental study of grouted sleeve connections under bending for steel modular buildings. Eng. Struct. **243**(112614), 110141–110296 (2021)

Dai, Z., Dai Pang, S., Liew, J.Y.R.: Axial load resistance of grouted sleeve connection for modular construction. Thin-Walled Struct. **154**(106883), 100263–108231 (2020)

Generalova, E.M., Generalov, V.P., Kuznetsova, A.A.: Modular buildings in modern construction. Procedia Eng. **153**(167–172), 1877–7058 (2016)

Huang, Z., Zhang, W., Fan, S., Sui, L., Ye, J.: Axial-load resistance of a novel UHPFRC grouted SHS tube-sleeve connection: experimental, numerical, and theoretical approaches. J. Struct. Eng. **147**(04021184), 04020733–04029445 (2021)

International, A.: ASTM C39/C39M-99-Standard Test Method for Compressive Strength of Cylindrical Concrete Specimens (ASTM International West Conshohocken) (1999)

Isa, M.N., Pilakoutas, K., Guadagnini, M.: Determination of tensile characteristics and design of eco-efficient UHPC. Structures **32**, 2174–2194 (2021)

Liew, J.Y.R., Chua, Y.S., Dai, Z.: Steel concrete composite systems for modular construction of high-rise buildings. Structures **21**, 135–149 (2019)

Lyu, W.-Q., Han, L.-H.: Investigation on bond strength between recycled aggregate concrete (RAC) and steel tube in RAC-filled steel tubes. J. Constr. Steel Res. **155**(438–459), 0143-0974X (2019)

Sanches, R., Mercan, O., Roberts, B.: Experimental investigations of vertical post-tensioned connection for modular steel structures. Eng. Struct. **175**(776–789), 0141–0296 (2018)

Singapore, B.C.A., Authority, C.: Design for manufacturing and assembly (DfMA): prefabricated prefinished volumetric construction. Singapore: Singapore BCA (2017)

Sui, L., Fan, S., Huang, Z., Zhang, W., Zhou, Y., Ye, J.: Load transfer mechanism of an unwelded, unbolted, grouted connection for prefabricated square tubular columns under axial loads. Eng. Struct. **222**(111088), 110141–110296 (2020)

Wang, L.-M., Wu, Y.-F.: Effect of corner radius on the performance of CFRP-confined square concrete columns: test. Eng. Struct. **30**(493–505), 0141–0296 (2008)

Wee, T.H., Chin, M.S., Mansur, M.A.: Stress-strain relationship of high-strength concrete in compression. J. Mater. Civ. Eng. **8**(70–76), 0899–1561 (1996)

Yokota, H., Rokugo, K., Sakata, N.: JSCE-2008 Recommendations for design and construction of high performance fiber reinforced cement composites with multiple fine cracks (HPFRCC). Jpn. Soc. Civ. Eng. (2008)

Zhang, W., Choo, Y.S., Yang, P., Shen, W., Huang, Z.: Nonlinear behaviour of fully grouted CHS X joints and associated representation for overall frame analysis. Thin-Walled Struct. **152**(106761), 100263–108231 (2020)